Available online at www.sciencedirect.com
ScienceDirect
Trans. Nonferrous Met. Soc. China 33(2023) 2866−2878
Transactions of Nonferrous Metals Society of China
www.tnmsc.cn

Distribution and evolution of particles in flash converting furnace under different operational conditions

Zhen-yu ZHU[1], Ping ZHOU[1], Zhuo CHEN[1], Jun ZHOU[2], Xing-bang WAN[1], Jing-song ZHANG[2], Peng REN[2]

1. School of Energy Science and Engineering, Central South University, Changsha 410083, China;
2. Tongling Non-ferrous Metals Group Co., Ltd., Tongling 244000, China

Received 4 October 2022; accepted 23 March 2023

Abstract: A series of industrial experiments were conducted, not only to reveal the distribution and evolution of particle mass and size inside the flash converting furnace, but also to investigate the influence of airflows on the particle distribution. The results showed that the average size of particles grows 2−3 times when falling through the reaction shaft, and large aggregated particles were mainly distributed in the center and outer part of the material cone. This phenomenon was attributed to the collision and aggregation of molten particles caused by the high turbulent intensity of airflow, high particle mass concentration, and positions of natural gas combusting. Moreover, increasing the momentum ratio of the distribution air to the process air helped the particles to be distributed more uniformly, which could be beneficial to matte oxidation. Compared with changing process air, adjusting the distribution air could improve the particle spatial distribution more efficiently.

Key words: industrial experiment; particle evolution; mass distribution; size distribution; momentum ratio; flash converting furnace

1 Introduction

The Kennecott−Outotec flash converting technology is known as a continuous process for the conversion of copper mattes into blister copper. Developed from the solid matte oxygen converting technology (known as SMOC) [1−3], it was initially created to deal with the challenge of keeping matte molten and flowing continuously. It has been implemented in five metallurgical plants in China in recent fifteen years [4,5].

Since flash converting technology started to be applied in the metallurgical process, related research has quickly followed. PÉREZ-TELLO et al [6−8] carried out a series of experiments and numerical computations in the early stage. They proposed the reactions that the copper matte particles experienced during the flash converting process and applied them in the numerical model to predict the reaction products. Besides, they used a compositional fragmentation model to investigate the size distribution and chemical composition of dust particles, revealing their fragmentation [9]. Various researches on the flash converting process were also carried out, including the freeze-lining formation [10], selenium and tellurium distribution behavior [11], and numerical modelling [12]. Apart from these, the thermal dynamics modelling of the flash converting process [13,14] and the formation mechanism of hazardous substances [15] were also investigated. Moreover, mechanism and computational studies, reviews of the process, or technical overviews of how to solve relative technical problems confronted in production practice were performed as well [16−18].

Various researches on the Kennecott−Outotec flash converting technology promote it to improve

Corresponding author: Zhuo CHEN, Tel: +86-13974891750, E-mail: chenzhuo@csu.edu.cn
DOI: 10.1016/S1003-6326(23)66304-6

continuously. So far, five flash converting furnaces in China produce 1950 kt of refined copper every year, which accounts for about 20% of total production in the country [19,20]. After several years of operation, the flash converting technology has brought many advantages, such as high efficiency for mass production, high operation rate of over 95%, high SO_2 concentration for acid-making, and high sulfur fixation rate. However, some drawbacks are also found in practice. For example, extra heat is needed to maintain the continuous process, and the corrosive calcium ferrite slag used in the process may result in a shorter life span of the furnace [19,21]. Apart from these problems, the ignition delay of particles gets severer as a higher feeding rate is generally to be achieved in modern production. The reason for ignition delay was considered to be the result of limited convective and radiative heat received by highly concentrated particles [22]. Therefore, understanding the distribution and evolution of the particles inside the furnace is essential to achieve good control of the reaction process, thus improving the product quality and prolonging the life span of the equipment.

The common methods to obtain the particle distribution inside the flash converting furnace (FCF) include experiments and computational fluid dynamic (CFD) simulation. Generally, the discrete phase model and population balance model are mostly used in CFD simulation to obtain the particle distribution and size evolution, respectively. However, as these two models could not be coupled, the particle trajectory [22,23] and agglomeration [24] were often investigated separately. For the experimental method, the literature on particle distribution in the FCF is rare. But as it is very similar to the flash smelting furnace (FSF) in terms of structure and operation mode, studies and results about the FSFs are usually borrowed and applied to the FCFs [25−28]. CHAUBAL [29] and HAHN [30] used the water-cooling sampler to collect particles at the bottom of a scaled reaction shaft and obtained the combustion process of concentrate in the FSF. Meanwhile, MUNROE [31] investigated the phenomenon of particle fragmentation and oxidation through the same method. By improving the sampler and applying it in industrial experiments, KIMURA et al [32] and KEMORI et al [33−35] found the particle growth and proposed the "two-particle model", which is different from the previous "fragmentation model" proposed by KIM [36], KIM and THEMELIS [37]. ZHOU and CHEN [38], and ZHOU [39] carried out the industrial experiment with the sink sampler under different conditions and thoroughly analyzed the oxidation and combustion process of the concentrate in the FSFs. The applications of the sink sampler helped researchers collect particles in the FSF and make investigations, which means that it should be also feasible in the research of the FCF.

In this work, the industrial experiment was carried out on the FCF under different operational conditions. The mass and size distributions of particles, including melted droplets and unmelted raw material particles, were analyzed so that the evolution of particles could be revealed. Meanwhile, how the operational parameters (i.e., airflow rates of the distribution air and the process air) influence the mass and size distributions of the particles were also figured out.

2 Experimental

2.1 Experimental method

The industrial experiment was performed in Jinguan Copper Co., Ltd. in Anhui Province, China. The schematic diagrams of the sampler and the sampling locations on the FCF used for the industrial sampling experiments are shown in Fig. 1. Originally, it was proposed to obtain the particle samples from three equidistant positions along the reaction shaft. However, considering the furnace structure and field space for sampling operation, only two holes were made at the heights of 2.1 and 3.9 m for the experiment, marked as H_1 and H_2 respectively in Fig. 1(a). The sampler used in the experiment is shown in Fig. 1(b). The stop point is used to remind the operators to stop pushing the sampler when this point reaches the outside wall of the furnace. The length from the sampler's tip to the stop point is the sum of the radius and the wall thickness of the reaction shaft. The ten sampler cells represent ten parts equally divided along the shaft radius.

During the experiment, in order to cool the sampler and quench the molten particle samples, the ten cells were initially filled with tap water around 300 K. Then, the sink sampler was quickly pushed into the reaction shaft, staying for 5−8 s,

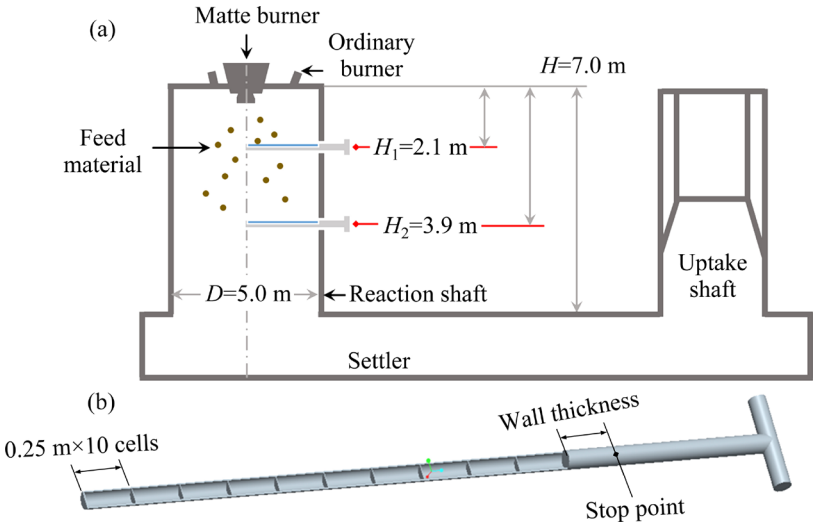

Fig. 1 Schematic diagrams of sampling holes (a) and sink sampler (b)

pulled out rapidly and poured with a large amount of water for further cooling. The sampling operation was repeated three times at one position under the same condition, so that the random error could be examined. Then, all samples were taken out from each cell and dried at a constant temperature of around 353 K in a vacuum drying oven. The dried samples were sealed in bags and labeled with positions for further analysis.

All the dried samples at different positions were sieved and weighed with an electronic balance to get the dry weight. In this work, four standard sieves of different sizes were used, and the corresponding sieve sizes are listed in Table 1. As large agglomerates were found in the samples, the standard sieve 1 was chosen to distinguish large agglomerates from the particles. Meanwhile, the other three sieves were used to determine size distribution of the sample.

Table 1 Standard sieve and corresponding sieve size

Standard sieve No.	1	2	3	4
Sieve pore size/μm	830	150	75	48

2.2 Operational parameters

The central jet distributed (CJD) burner is commonly used in the FCFs. Figure 2 gives a schematic showing how the gases and feed materials flow through the CJD matte burner into the reaction shaft. Notably, three airflows are fed into the furnace, supplying oxygen for the reactions and creating turbulence to facilitate interactions between the gaseous and granular phases. Among

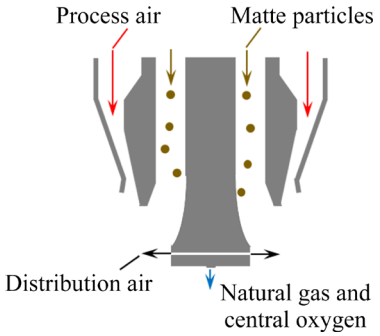

Fig. 2 Schematic diagram of matte burner with different inlets

them, the vertical process air is helpful to envelop the particles and avoid the lining being eroded by material particles [23]. The distribution air is aimed to blow the granules horizontally, making them distributed more uniformly in the reaction shaft. Based on the hydrodynamic effect of these two airflows, the concept of the momentum ratio of the distribution air to the process air ($K_{d/p}$) was proposed by the research group to measure the effects of two airflows on the distribution of material particles [23]. It can be calculated as Eq. (1), which indicates that the larger the $K_{d/p}$ is, the more dispersed the particles are.

$$K_{d/p}=\frac{I_d}{I_p}=\frac{q_{m,d}v_d}{q_{m,p}v_p} \tag{1}$$

where I, q_m, and v denote the momentum, mass flow rate, and velocity, respectively; subscripts "d" and "p" denote the distribution air and process air, respectively.

The industrial experiments were carried out

under four conditions to investigate the influences of airflows on the particle distributions, and the operational parameters are shown in Table 2. In the four experimental conditions, the operational parameters of the reference condition are the typical and common ones adopted in normal production. The D-high, P-low, and D&P-low conditions are set as the control groups, of which the D and P come from the initial letter of the terms "distribution air" and the "process air", respectively, and the high and low indicate the level of the airflow rates compared to the reference condition.

The original purpose of setting the control groups is to investigate how the distribution air and the process air act on the particle dispersion under a higher $K_{d/p}$. However, it was difficult to achieve the same high value of $K_{d/p}$ under both the D-high and the P-low conditions, because the difference between the two airflow rates was too large and the safety of industrial production had to be considered. As a result, different $K_{d/p}$ values were obtained by adequately increasing the airflow rates in two conditions. The D&P-low condition was set to check whether the same particle distribution could be achieved with the lower flowrate, which kept $K_{d/p}$ at the same value as the reference condition.

3 Results and discussion

3.1 Particle mass and size distributions

3.1.1 Mass distribution

When the raw materials are fed into the reaction shaft, particles are quickly dispersed but still distributed in the center of the reaction shaft, thus forming a bell-shaped particle-dense region, which is usually called the "material cone" in practice, as illustrated in Fig. 3. Since the cross-section of the cone is not a standard circle, the concept of the "radius of the material cone" was proposed, for the convenience of describing and comparing the dispersed degree of particles. In definition, R_{99} is the radius of an equivalent circle, through which the particle mass is 99% of the total mass on the cross-section of the material cone at one height.

The statistical data of R_{99} in the reference condition are given in Table 3, which is the average of three sampling tests in one condition. It can be found that the standard deviation and coefficient of variation at two sampling heights are small enough, which indicates that the sampling results of mass distribution vary slightly during the experiments.

The particle mass distribution at different heights of the reaction shaft under the reference condition is shown in Fig. 4. As it is difficult to have the same sample mass at different sampling locations, to make the results more convincing, the mass weight of the samples in each cell is changed into the mass fraction according to Eq. (2):

$$c_i = \left(m_i / \sum_{i=1}^{10} m_i \right) \times 100\% \tag{2}$$

where c_i is the mass fraction in cell i, and m_i is the mass of samples in cell i.

From Fig. 4, it can be seen that the samples mainly distribute within the reaction shaft radius range of R=0−0.75 m at the height of H_1=2.1 m and within the range of R=0−1.00 m at H_2=3.9 m. And the mass distributions at two heights exhibit different trends. At the height of H_1, the mass fraction increases initially, and then followed by a decrease, and the peak occurs at R=0.25−0.50 m. As for the mass distribution at H_2, it decreases initially, followed by an increase, but then decreases again, and two peaks occur at R=0−0.25 m and R= 0.75−1.00 m, respectively. The trend of mass distribution at H_2 is similar to the result at R_2 in the research on FSF [38], indicating that the mass fraction in the reaction shaft is large in the center part of the material cone and fluctuates in the outer part.

Table 2 Specific operational parameters in experimental conditions

Condition	Load of matte/ ($t \cdot h^{-1}$)	Load of ash/ ($t \cdot h^{-1}$)	Air volume of process air/ ($m^3 \cdot h^{-1}$)	Oxygen volume of process air/ ($m^3 \cdot h^{-1}$)	Velocity of process air/($m \cdot s^{-1}$)	Volume of distribution air/($m^3 \cdot h^{-1}$)	Volume of central oxygen/ ($m^3 \cdot h^{-1}$)	Volume of central CH_4/ ($m^3 \cdot h^{-1}$)	$K_{d/p}$
Reference	85	6	3500	12950	88	1000	1050	150	0.1018
D-high	85	6	3500	12950	88	1500	1050	150	0.229
P-low	85	6	2500	12950	70	1000	1050	150	0.1363
D&P-low	85	6	3327	12307	75	900	1050	150	0.1018

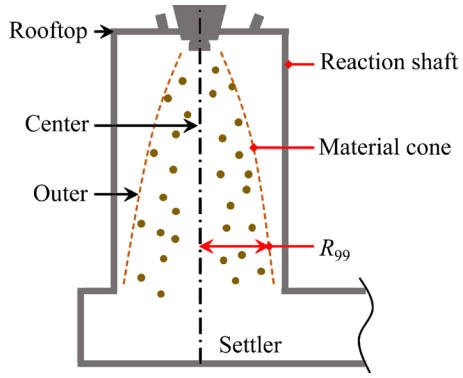

Fig. 3 Schematic diagram showing material cone and R_{99}

Table 3 Radius of material cone R_{99} in reference condition

Height/m	Mean/m	SD/m	CV/%
2.1 (H_1)	0.94	0.036	3.84
3.9 (H_2)	1.31	0.064	4.87

SD: Standard deviation; CV: Coefficient of variation

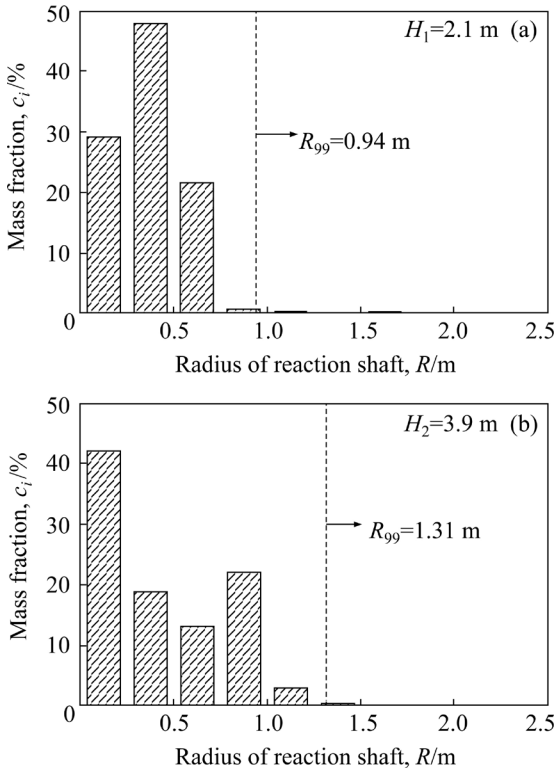

Fig. 4 Mass distribution of samples in reference condition

3.1.2 Particle size distribution

To investigate the particle size distribution (d_p) of samples, the matte particles fed into the furnace were sieved beforehand as a reference, which is shown in Fig. 5(a). The size distribution of samples is presented in Figs. 5(b_1, b_2). It can be seen that

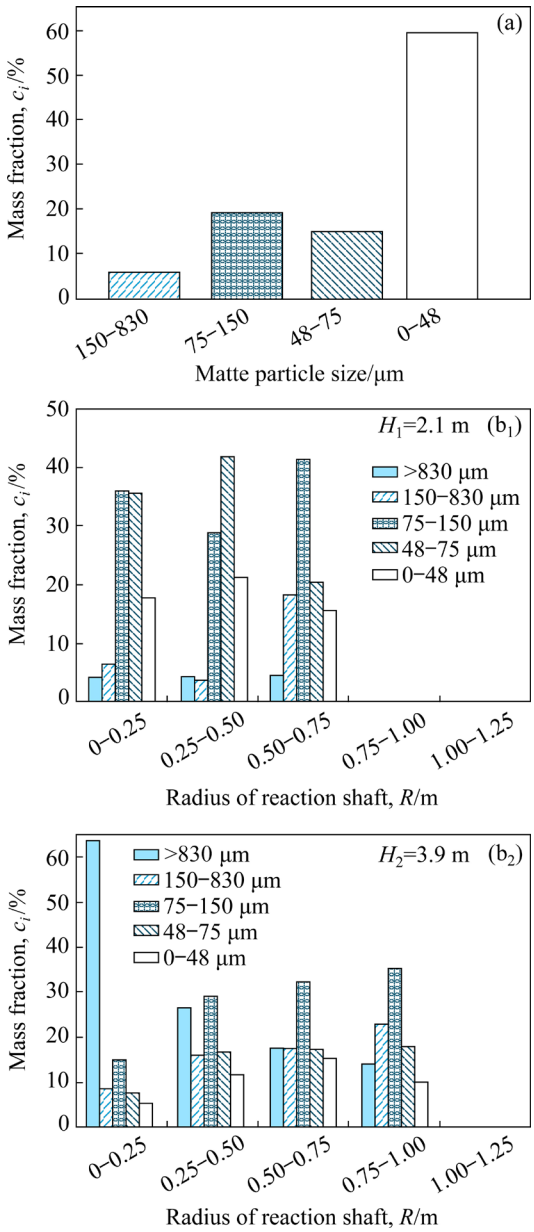

Fig. 5 Particle size distribution of matte (a) and samples (b_1, b_2) in reference condition

59.5 wt.% of the matte particles are smaller than 48 μm. Compared with it, the sample size in the reference condition increases, but the largest fractions in each cell are not the same. Meanwhile, the sample particles aggregated into a new size range larger than 830 μm since it does not exist in Fig. 5(a).

At the height of H_1, the mass fractions of $d_p > 830$ μm in three cells have a similar value of around 4%. The sample particles with sizes of 75 μm < d_p < 150 μm and 150 μm < d_p < 830 μm are mainly concentrated in the cells of R=0−0.25 m and R=0.50−0.75 m, respectively, while the small

particles with sizes of $0 < d_p < 48$ μm and $48 < d_p < 75$ μm are concentrated in the radial range of R=0.25−0.50 m. This means that the sample particles in the center and the outer parts of the material cone are larger than those in the middle section, even though all these samples show an increasing trend in particle size.

At the height of H_2, the mass fraction of $d_p > 830$ μm is extremely large in the cell with R=0−0.25 m, which reaches 65%, and it gradually goes down in the cell with R=0.25−1.00 m. However, the mass fractions of particles in the range from 48 to 830 μm increase gradually within the radius of R=0−1.00 m. As for the particles of $d_p < 48$ μm, the mass fractions in the cell of R=0−0.25 m and R=0.75−1.00 m are lower. This means that the particles at this height are still larger in the center and outer parts of the material cone and smaller in the middle section.

Moreover, apart from the particle size above 830 μm, the particles in a size range of $75\ \mu m < d_p < 150\ \mu m$ always have the largest mass fractions. This indicates that a large part of the matte particles ($d_p < 48$ μm, the main size according to Fig. 5(a)) are more likely to aggregate into particles that are 2−3 times larger when flowing through the reaction shaft.

The mean diameter was calculated according to Eq. (3) to quantify the particle size distribution, and related statistical data in three tests are given in Table 4. On the one hand, the mean diameters show an upward trend along the axial direction of the reaction shaft. The change in the mean sizes at the two heights indicates that the growth in the particle size mainly occurs in the center and outer sections of the material cone. On the other hand, the most significant coefficient of variation is less than 15%, indicating that the deviation is small enough to guarantee reproducibility in this industrial experiment.

$$\overline{D} = \sum_{n=1}^{4} \frac{1}{2}\left(S_{n,\min} + S_{n,\max}\right)p_n + S_{5,\min}\,p_5 \tag{3}$$

where $\overline{D}$ is the mean diameter of particles, $S_{n,\min}$ and $S_{n,\max}$ are the minimum and the maximum values in one range of particle size (e.g., 0 and 48 μm, respectively in Fig. 5), n is the number of the size range, and p_n is the mass fraction of corresponding range, $S_{5,\min}$ is 830 μm, and p_5 is the mass fraction of $S_{5,\min}$.

Table 4 Mean diameter of particles in reference condition

Height/m	R/m	Mean/μm	SD/μm	CV/%
2.1 (H_1)	0−0.25	132.58	9.63	7.26
	0.25−0.50	123.08	7.19	5.84
	0.50−0.75	194.49	7.14	3.67
3.9 (H_2)	0−0.25	573.2	27.44	4.79
	0.25−0.50	302.04	32.48	10.75
	0.50−0.75	265.45	22.98	8.66
	0.75−1.00	279.15	3.75	1.34

SD: Standard deviation; CV: Coefficient of variation

Compared with the mean value of matte particles (74.37 μm), the size of sample particles increased at both heights of 2.1 and 3.9 m. This size-growing phenomenon of particles is also found in the industrial measurement of FSF [7,33,38]. Notably, the decrease of the mean diameters along the radius at H_2 is the same as the result of R_2 in the experiment of FSF [38]. To further investigate the coarser particle, the morphology of samples was examined. The typical morphologies of samples at two heights are shown in Fig. 6. It can be found that the large particles at H_1 are mostly the agglomerates of fine particles, demonstrated in Fig. 6(a). While at the height of H_2, the large spherical particles with smooth rims could be observed (shown in Fig. 6(b)), which means that large fused particles with a higher molten state started to appear.

Overall, by comparing the size distribution and investigating the morphology of large particles, the evolution of particle size can be summarized into three aspects. Firstly, small particles may have melted at the height of H_1=2.1 m and some of them agglomerate into larger ones when further falling through the reaction shaft. Secondly, the large fused particles in a high molten state appear at H_2=3.9 m. Thirdly, the particle size growing phenomenon is more obvious in the center and outer parts of the material cone, indicating that particles are heated and react faster in these sections.

3.1.3 Evolution of particles

Based on the above analysis of the spatial distribution of particle mass and size, the evolution of material particles during the process of falling through the reaction shaft can be summarized and illustrated in Fig. 7. The initial height H_0 is also included, and the distributed radius at H_0 is

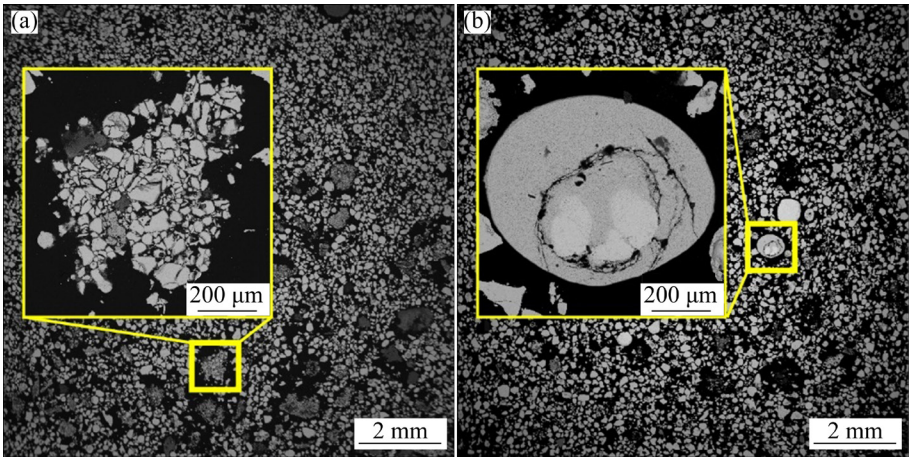

Fig. 6 Morphologies of samples at heights of H_1=2.1 m (a) and H_2=3.9 m (b)

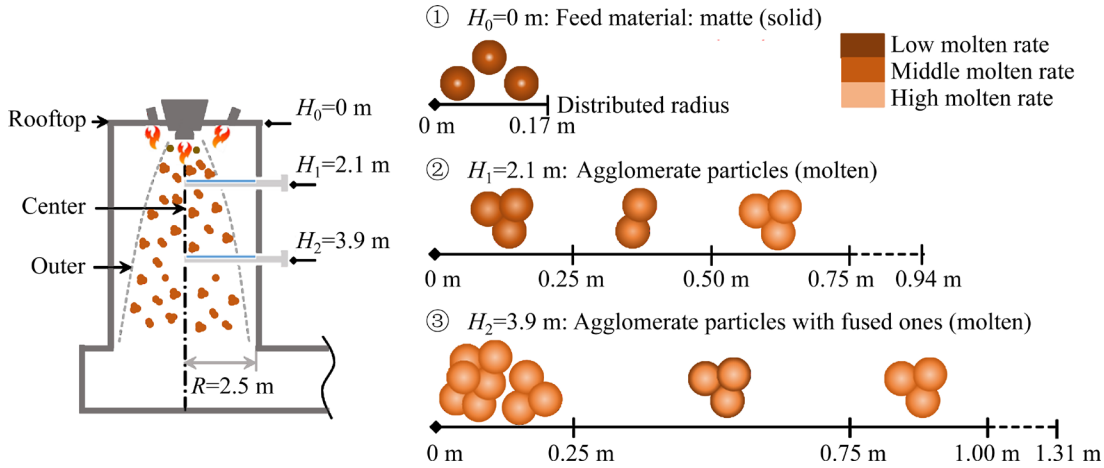

Fig. 7 Particle evolution in falling process

determined according to the size of discharging chute. During the matte falling process, the outer line of the material cone could be sketched by distributed radii at different heights, as shown in Fig. 7. The radius of the material cone increases fast initially, reaching 0.94 m at H_1=2.1 m, then the increasing rate slows down, reaching 1.31 m at H_2=3.9 m, and might increase to 2.5 m at the bottom of the reaction shaft.

In this flash converting furnace, extra heat is needed to maintain the continuous reactions of the process. Therefore, except for using the ordinary burners at the rooftop of the reaction shaft, natural gas was also supplied through the matte burner (as shown in Figs. 2 and 7). The combustion of natural gas causes the matte particles in the center and outer parts of the material cone to be ignited and melted quickly. The small molten particles agglomerate into large particles at least from the height of 2.1 m, while large fused particles appear at the height of 3.9 m. The reason for particle size growth along the reaction shaft is attributed to the high airflow turbulence and particle mass concentration. PÉREZ-TELLO et al [40] thought that airflow turbulence could create severer collision, and the collision of molten particles directly led to aggregation. Notably, ZHOU et al [23] stated that the particle growth in the outer of the material cone could be mainly caused by the high-speed process air and turbulence intensity. While for the particle growth in the center part of the reaction shaft, the main reason is considered to be the high mass concentration that leads to particle collision, which is elaborated in the literature [41].

3.2 Influence of operational parameters on material distribution

3.2.1 Influence on particle mass distribution

The sieving results for the particle mass distribution under four different conditions are shown in Fig. 8. Also, the result of the reference condition is included as a comparison. Meanwhile,

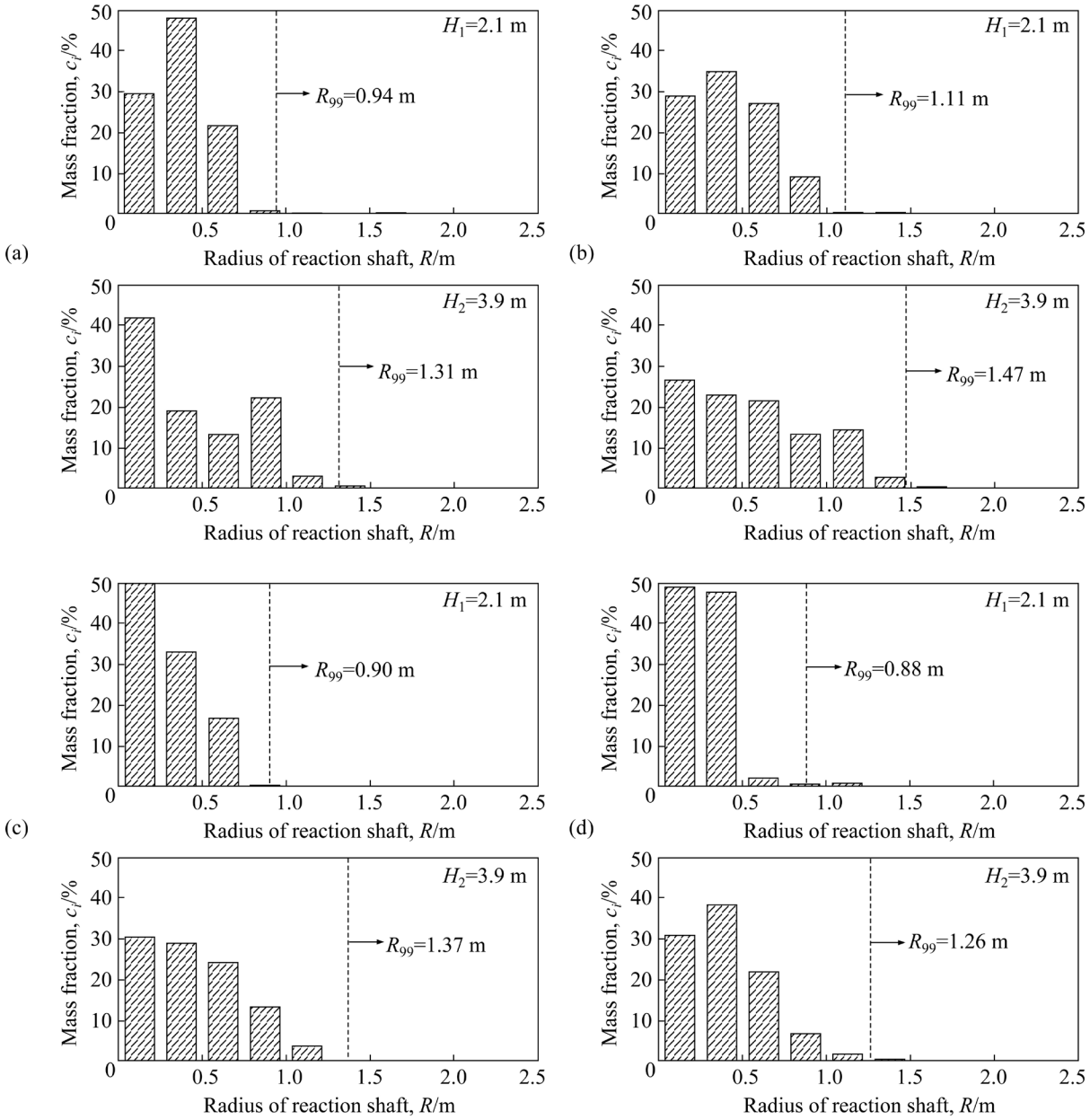

Fig. 8 Mass distribution under different conditions: (a) Reference; (b) D-high; (c) P-low; (d) D&P-low

the variances of the mass fraction c_i at each height are calculated and shown in Table 5. It should be noted that the mass fraction less than 5% was not counted, e.g., only samples in the first three cells were considered at H_1 in the reference condition.

By comparing the result in Fig. 8(b) with that in Fig. 8(a), it can be found that the R_{99} at the height of H_1 increases from 0.94 m in the reference condition to 1.11 m in the D-high condition, and the value at the height of H_2 increases from 1.31 m in the reference condition to 1.47 m in the D-high condition. Obviously, by increasing the flowrate of the distribution air, more horizontal momentum is to be acted on the particles, causing the material cone to expand larger. Meanwhile, the changing trends of the particle mass distribution in these two conditions are similar. At the height of H_1, the particle mass fraction increases initially, followed by a decrease, and the peak still occurs at R=0.25−0.50 m. While the mass fraction at H_2 decreases initially, followed by an increase, but then decreases again; the first peak appears at R=0−0.25 m and the second peak changes from R=0.75−1.00 m to R=1.00−1.25 m. What's more, according to Table 5, the variances in the D-high condition are smaller, which indicates that the mass fraction in this condition becomes more uniform no matter at the height of H_1 or H_2. In contrast, the

particle mass in the reference condition is relatively centralized, specifically at R=0.25−0.50 m of H_1 and R=0−0.25 m of H_2. Thus, it can be concluded that the particles have a larger dispersion radius and become more uniform in the reaction shaft after increasing the distribution air.

Table 5 Variances of dimensionless parameter c_i at each height

Height/m	Condition	Sample numbers	Variance
2.1 (H_1)	Reference	3	0.0182
	D-high	4	0.0121
	P-low	3	0.0274
	D&P-low	2	−
3.9 (H_2)	Reference	4	0.0155
	D-high	5	0.0033
	P-low	4	0.0060
	D&P-low	4	0.0186

Comparing the result of the P-low condition in Fig. 8(c) with that of the reference condition, the radius of the material cone changes a little, i.e., the R_{99} at the height of H_1 decreases from 0.94 m in the reference condition to 0.90 m in the P-low condition, and the R_{99} at the height of H_2 increases from 1.31 to 1.37 m. However, the trend of the particle mass fraction in the P-low condition is different from that in the reference condition, as the mass fractions decrease gradually at both heights of H_1 and H_2, from R=0 m to R=2.50 m. There are two reasons for this. Firstly, the increase of the $K_{d/p}$ is not large enough, so the R_{99} does not change much. Secondly, the influence of the process air on the particle distribution is limited in the outer part of the material cone. Therefore, even though the $K_{d/p}$ increases, decreasing the velocity of process air shows a minimal influence on the particle distribution in the reaction shaft.

Last but not the least, the result of the D&P-low condition in Fig. 8(d) shows its unique character on the particle distribution. Firstly, the R_{99} in the D&P-low condition is smaller than that in other three conditions; the values at the heights of H_1 and H_2 are 0.88 and 1.26 m, respectively. Meanwhile, the sample at H_1 is concentrated in the cells with R=0−0.50 m, as the mass fraction nearly reaches 50% in the first two cells. Moreover, the mass fraction at H_2 increases initially, then decreases, and the maximum value occurs at R=0.25−0.50 m. Therefore, even if the $K_{d/p}$ was kept at the same value, reducing the airflow rate and velocity would make particles gather in the center of the reaction shaft, which is a worse dispersion. This phenomenon was also observed in the numerical work of FSF [23], which means that maintaining a large airflow rate is essential to particle distribution and reaction.

3.2.2 Influence on particle size distribution

From the analysis in Subsection 3.1, it has been deduced that the molten particles would aggregate into large ones, leading to an increase in particle size. Hence, the particle size distribution in each condition can to some extent reflect the molten degree and the reaction process of the particles. As the mass distribution has been discussed above, the particle size distribution of samples in each condition is accordingly given in Fig. 9. Meanwhile, to obtain a more specific change of the sample diameter, the mean diameters $\overline{D}$ in each position are calculated according to Eq. (3) and listed in Table 6.

Comparing the particle size distribution in the reference condition with the D-high condition (shown in Figs. 9(a) and (b)), it can be found that the particle size in the D-high condition is larger at the height of H_1, but it has a similar size distribution at the height of H_2 with that in the reference condition. Specifically, at the height of H_1, the mass fraction of particles with a diameter of d_p > 150 μm increases a lot, especially the mass fraction of d_p > 830 μm in the cell with R=0−0.25 m takes up to 38.57%. Meanwhile, in the cell with R=0.50−0.75 m, the particle in size of 75 < d_p < 150 μm takes the largest fraction, 42.06%. According to the data in Table 6, it can be found that the mean diameters of particles at R=0−0.25 m, R=0.25−0.50 m, and R=0.50−0.75 m are 415.5, 276.2, and 310.6 μm, respectively. Compared to the reference condition, the growth rates of mean diameters are 3.1, 2.2, and 1.6, respectively. Therefore, two conclusions can be concluded. Firstly, as the mean diameters are larger at R=0−0.25 m and R=0.50−0.75 m, there should be enough heat and strong turbulence in these regions, causing the particles to aggregate into larger ones. Secondly, the decline of particle growth rates represents that increasing the distribution air will significantly influence the particles in the center

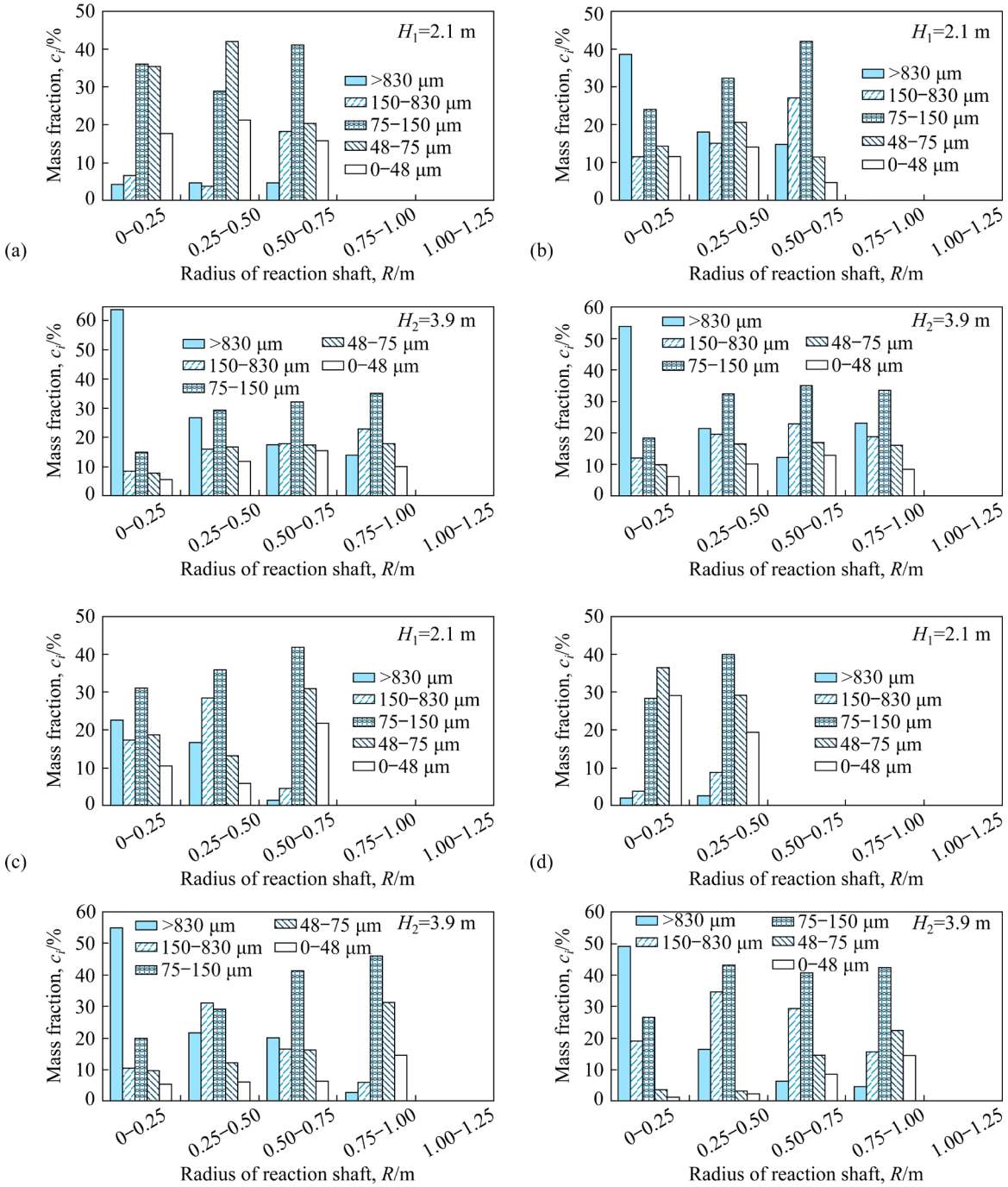

Fig. 9 Particle size distribution of samples under different conditions: (a) Reference; (b) D-high; (c) P-low; (d) D&P-low

Table 6 Mean diameters of samples in different conditions

Condition	$\bar{D}$ at H_1/μm			$\bar{D}$ at H_2/μm			
	R= 0−0.25 m	R= 0.25−0.50 m	R= 0.50−0.75 m	R= 0−0.25 m	R= 0.25−0.50 m	R= 0.50−0.75 m	R= 0.75−1.00 m
Reference	132.6	123.1	194.5	573.2	302	265.5	279.2
D-high	415.5	276.2	310.6	533.4	323	266.4	332.9
P-low	321.4	326.9	103.9	535.3	373.7	304.3	125.2
D&P-low	97.1	132.7	–	534.9	357.8	354.5	182.5

part of the material cone. At the height of H_2, the particle size distribution and mean diameter between the reference and D-high conditions are similar. Therefore, it can be concluded that increasing the distribution air would lead to particle size growth, especially at the height of H_1=2.1 m, but the influence is limited at the height of H_2.

The size distribution of samples in the P-low condition is shown in Fig. 9(c). It can be found that the mass fraction of particles in a size of d_p > 150 μm becomes larger when approaching the center of the reaction shaft. Comparing the results of the P-low and the reference conditions, several differences can be found at the heights of H_1 and H_2. Firstly, at H_1, the mass fraction of particles with size of d_p > 150 μm is higher at R=0−0.25 m and R=0.25−0.50 m, while it is lower at R=0.50−0.75 m. These cells that obtained larger particles are contrary to the reference condition, which means that reducing the velocity of process air may weaken the influence of the process air on the outer part of the material cone. However, simultaneously, as the particle size increases at R=0−0.25 m and R=0.25−0.50 m, the effect of the distribution air in the center part is strengthened. Then, at the height of H_2, one clear difference between these two conditions is that the mass fraction of particles with the size of d_p < 75 μm becomes larger at R=0.75−1.00 m, which is corresponding to the small particle size at R=0.50−0.75 m of H_1. Taking the results in Table 6 into consideration, the mean diameters of the first two cells at H_1 increase. This growth indicates that decreasing the velocity of the process air may have a weak influence on the center part but may not be good for the sample in the outer part of the material cone.

As shown in Fig. 9(d) and Table 6, the particle size is smaller in the D&P-low condition than the result of the reference condition. Firstly, at H_1, the particle sizes (d_p < 150 μm) take large mass fractions, leading to the mean diameter at R=0−0.25 m being smaller than that in the reference condition. This means that decreasing both the distribution air and the process air will lead to the decrease of particle size as the intensity of the turbulence is weakened. Then, at H_2, it can be found that, at R=0−0.25 m and R=0.25−0.50 m, the mass fraction of d_p < 75 μm in the D&P-low condition is lower than that in the reference condition. Combined with the result of the mass fraction, the reason is supposed to be that the radius of the material cone becomes smaller so that the high mass concentration leads to a greater probability of particle colliding and aggregating. However, at R=0.50−0.75 m and R=0.75−1.00 m, the particle mass fraction (d_p > 830 μm) in the D&P-low condition is low, and the mean diameter at R=0.75−1.00 m is 182.5 μm, which is smaller than 279.2 μm in the reference condition. Therefore, it is assumed that decreasing the airflow rate will lead to the decline of turbulent intensity, which reduces the chance of collision and aggregation.

4 Conclusions

(1) The evolution of particles in the reaction shaft was summarized by analyzing the particle mass and size distributions in the reference condition. It is found that particles in the center and the outer parts of the material cone are usually larger. The mean diameter started growing at least from the height of 2.1 m and showed an upward trend along the axial direction of the reaction shaft. Moreover, the molten particles collided into large agglomerates at 2.1 m, while some fused particles were found at 3.9 m.

(2) The reason leading to the unequal particle size growing in the reaction shaft was attributed to the high intensity of airflow turbulence and high particle mass fraction. Meanwhile, the combustion of natural gas from the matte burner and ordinary burners may play a crucial role in the position of particle ignition and deformation.

(3) When falling through the reaction shaft, apart from the particle size above 830 μm, particles with a size of 75 μm < d_p < 150 μm take up the largest mass fraction, indicating that a large part of the matte particles (d_p < 48 μm, the main matte size) will aggregate into particles that are 2−3 times larger than those inside the reaction shaft.

(4) Increasing the momentum ratio of airflows helps the particles to be distributed more uniformly in the reaction shaft, which could be beneficial to the matte oxidation. Furthermore, adjusting the distribution air to increase the momentum ratio will achieve a better result than changing the process air.

Acknowledgments

The authors are grateful for the financial support from the National Natural Science

Foundation of China (No. 2106217). We also appreciate Jinguan Copper Co., Ltd. for its technical support in the field experiments. Many thanks especially to Prof. Jun ZHOU for his advice on the experimental plan, and Peng REN, Shu-feng YE, and Zhi-nan XING for their great help in the experiment.

References

[1] ASTELJOKI J A, BAILEY L K, GEORGE D B, RODOLFF D W. Flash converting—Continuous converting of copper mattes [J]. JOM, 1985, 37(5): 20−23.

[2] KOJO I V, JOKILAAKSO A, HANNIALA P. Flash smelting and converting furnaces: A 50-year retrospect [J]. JOM, 2000, 52(2): 57−61.

[3] KOJO I V, JOKILAAKSO A, HANNIALA P. Outokumpu flash smelting technology and the production network concept [C]//JOËL K, TONY W. International Peirce-Smith Converting Centennial. San Francisco, CA: TMS, 2000: 606−612.

[4] GEORGE D B, NEXHIP C, GEORGE-KENNEDY D, FOSTER R, WALTON R. Copper matte granulation at the Kennecott Utah copper smelter [C]//CAMERON H, HANI H, TONY W. Granulation of Molten Materials. San Francisco, CA: TMS, 2006.

[5] ZHOU Jun. An overview on flash converting technology [J]. Nonferrous Metals Engineering, 2011, 1(1): 30−36. (in Chinese)

[6] PÉREZ-TELLO M. Experimental investigation and computer simulation of the continuous flash converting process of solid copper mattes [D]. Utah, USA: The University of Utah, 1999.

[7] PÉREZ-TELLO M, SOHN H Y, MARIE K S, JOKILAAKSO A. Experimental investigation and three-dimensional computational fluid-dynamics modeling of the flash-converting furnace shaft: Part I. Experimental observation of copper converting reactions in terms of converting rate, converting quality, changes in particle size, morphology, and mineralogy [J]. Metallurgical and Materials Transactions B, 2001, 32(5): 847−868.

[8] PÉREZ-TELLO M, PARRA-SÁNCHEZ V R, SÁNCHEZ-CORRALES V M, GÓMEZ-ÁLVAREZ A, BROWN-BOJÓRQUEZ F, PARRA-FIGUEROA R A, BALLADARES-VARELA E R, ARANEDA-HERNÁNDEZ E A. Evolution of size and chemical composition of copper concentrate particles oxidized under simulated flash smelting conditions [J]. Metallurgical and Materials Transactions B, 2018, 49(2): 627−643.

[9] DUARTE-RUIZ C A, PÉREZ-TELLO M, PARRA-SÁNCHEZ V R, SOHN H Y. The role of expansion and fragmentation phenomena on the generation and chemical composition of dust particles in a flash converting reactor [J]. Metallurgical and Materials Transactions B, 2016, 47(5): 3115−3125.

[10] FALLAH-MEHRJARDI A, JANSSON J, TASKINEN P, HAYES C P, JAK E. Investigation of the freeze-lining formed in an industrial copper converting calcium ferrite slag [J]. Metallurgical and Materials Transactions B, 2014, 45(3): 864−874.

[11] YU F, LIU Z, YE F, XIA L, JOKILAAKSO A. A study of selenium and tellurium distribution behavior, taking the copper matte flash converting process as the background [J]. JOM, 2021, 73(2): 694−702.

[12] TASKINEN P, JOKILAAKSO A. Reaction sequences in flash smelting and converting furnaces: An in-depth view [J]. Metallurgical and Materials Transactions B, 2021, 52(5): 1−19.

[13] SWINBOURNE D R, KHO T S. Computational thermodynamics modeling of minor element distributions during copper flash converting [J]. Metallurgical and Materials Transactions B, 2012, 43(4): 823−829.

[14] LI Ming-zhou, ZHOU Jie-min, TONG Chang-ren, ZHANG Wen-hai, CHEN Zhuo, WANG Jin-liang. Thermodynamic modeling and optimization of the copper flash converting process using the equilibrium constant method [J]. Metallurgical and Materials Transactions B, 2018, 49(4): 1794−1807.

[15] ZHOU Hui-hui, LIU Gui-jian, ZHANG Li-qun, ZHOU Chun-cai. Formation mechanism of arsenic-containing dust in the flue gas cleaning process of flash copper pyrometallurgy: A quantitative identification of arsenic speciation [J]. Chemical Engineering Journal, 2021, 423: 130193.

[16] SUN Lai-sheng, CHAI Man-lin, MENG Fan-wei. Plant practice of “Double-Flash” copper smelting in tongling nonferrous metals [J]. Nonferrous Metals (Extractive Metallurgy), 2015(9): 10−14. (in Chinese)

[17] YU Feng, XIA Long-gong, ZHU Yin-bin, JOKILAAKSO A, LIU Zhi-hong. Reaction behavior of Na_2SO_4-containing copper matte powders in a simulated flash converting process [J]. Metallurgical and Materials Transactions B, 2021, 52(5): 3468−3476.

[18] MENG Fan-wei. Practice on trial production of flash converting for Jinguan Copper Corporation [J]. Nonferrous Metals Engineering & Research, 2015, 36(5): 25−27, 30. (in Chinese)

[19] LIU Zhi-hong, XIA Long-gong. The practice of copper matte converting in China [J]. Mineral Processing and Extractive Metallurgy, 2019, 128(1/2): 117−124.

[20] WAN Ai-dong, GUO Wan-shu, ZHANG Geng-sheng, ZHANG Jian-ping, XIE Xiao-feng. Characteristics and production operation of flash smelting furnace [J]. Nonferrous Metallurgical Equipment, 2017(1): 52−57. (in Chinese)

[21] ZHOU Jun. Theory and practice of process control in matte flash converting [J]. Nonferrous Metals (Extractive Metallurgy), 2017(10): 1−9. (in Chinese)

[22] GAO Dong-bo, PENG Xiao-qi, SONG Yan-po, ZHU Zhen-yu, DAI Yang. Mathematical modelling and numerical optimization of particle heating process in copper flash furnace [J]. Transactions of Nonferrous Metals Society of China, 2021, 31(5): 1506−1517.

[23] ZHOU Jun, ZHOU Jie-min, CHEN Zhuo, MAO Yong-ning. Influence analysis of air flow momentum on concentrate dispersion and combustion in copper flash smelting furnace

by CFD Simulation [J]. JOM, 2014, 66(9):1629−1637.
[24] HIGGINS D, GRAY N, DAVIDSON M. Simulating particle agglomeration in the flash smelting reaction shaft [J]. Minerals Engineering, 2009, 22(14): 1251−1265.
[25] LI Xin-feng, MEI Chi, ZHOU Ping, HAN Xiang-li, XIAO Tian-yuan. Mathematical model of multistage and multiphase chemical reactions in flash furnace [J]. Transactions of Nonferrous Metals Society of China, 2003, 13(1): 203−207.
[26] CHEN Hong-rong, MEI Chi, XIE Kai, LI Xing-fen, ZHOU Jun, WANG Xiao-hua. Operation optimization of concentrate burner in copper flash smelting furnace [J]. Transactions of Nonferrous Metals Society of China, 2004, 14(3): 631−636.
[27] CHEN Zhuo, ZHU Zhen-yu, WANG Xiao-na, SONG Yan-po. Online monitoring and assessment of energy efficiency for copper smelting process [J]. Journal of Central South University, 2019, 26(8): 2149−2159.
[28] AI Yuan-fang, SUN Yan-wen, CHEN Hong-rong, LIU an-ming. Cold model experiment for particle distribution of CJD burner [J]. Journal of Northeastern University (Natural Science), 2014, 35(4): 543−547. (in Chinese)
[29] CHAUBAL P C. The reaction of chalcopyrite concentrate particles in a flash furnace shaft [D]. Utah, USA: University of Utah, 1986.
[30] HAHN Y B. Mathematical modeling of chalcopyrite concentrate combustion in an axisymmetric flash-furnace shaft [D]. Utah, USA: University of Utah, 1988.
[31] MUNROE N D H. Simulation of flash smelting phenomena in a laboratory reactor [D]. New York: Columbia University, 1987.
[32] KIMURA T, OJIMA Y, MORI Y. Reaction mechanism in a flash smelting reaction shaft [C]//GASKELL D R, HAGER J P, HOFFMANN J E. International Symposium on Innovative Technology and Reactor Design in Extraction Metallurgy. Warrendale, PA: TMS-AIME, 1986: 403−418.
[33] KEMORI N, DENHOLM W T, KUROKAWA H. Reaction mechanism in a copper flash smelting furnace [J]. Metallurgical and Materials Transactions B, 1989, 20(3): 327−336.
[34] KEMORI N, SHIBATA Y, FUKUSHIMA K. Thermodynamic consideration for oxygen pressure in a copper flash smelting furnace at Toyo Smelter [J]. JOM, 1985, 37(5): 24−29.
[35] KEMORI N, SHIBATA Y, TOMONO M. Measurements of oxygen pressure in a copper flash smelting furnace by an Emf method [J]. Metallurgical and Materials Transactions B, 1986, 17(3): 111−117.
[36] KIM Y H. Studies of the rate phenomena in particulate flash reaction systems: Oxidation of metal sulfides [D]. New York: Columbia University, 1987.
[37] KIM Y H, THEMELIS N J. Effect of phase transformation and particle fragmentation on the flash reaction of complex metal sulfides [C]//GASKELL D R, HAGER J P, HOFFMANN J E. International Symposium on Innovative Technology and Reactor Design in Extraction Metallurgy. Warrendale, PA: TMS-AIME, 1986: 349−369.
[38] ZHOU Jun, CHEN Zhuo. Smelting mechanism in the reaction shaft of a commercial copper flash furnace [C]// DAVIS B. Extraction 2018. The Minerals, Metals & Materials Series. Cham: Springer, 2018: 533−546.
[39] ZHOU Jun. Studies of metallurgical processes in flash smelting with high intensity [D]. Changsha: Central South University, 2015. (in Chinese)
[40] PÉREZ-TELLO M, SOHN H Y, SMITH P J. Experimental investigation and three-dimensional computational fluid-dynamics modeling of the flash-converting furnace shaft: Part II. Formulation of three-dimensional computational fluid-dynamics model incorporating the particle-cloud description [J]. Metallurgical and Materials Transactions B, 2001, 32(5): 869−886.
[41] TASKINEN P, JOKILAAKSO A, LINDBERG D, XIA J L. Modelling copper smelting — The flash smelting plant, process and equipment [J]. Mineral Processing and Extractive Metallurgy, 2020, 129(2): 207−220.

闪速吹炼炉内颗粒在不同操作参数下的分布与演化规律

祝振宇[1]，周 萍[1]，陈 卓[1]，周 俊[2]，万兴邦[1]，张劲松[2]，任 鹏[2]

1. 中南大学 能源科学与工程学院，长沙 410083；
2. 铜陵有色金属集团控股有限公司，铜陵 244000

摘 要：通过开展工业试验揭示闪速吹炼炉内颗粒质量和粒径的分布与演化规律，同时研究不同配风参数对颗粒分布的影响。结果表明，颗粒在反应塔内的下落过程中，其平均粒径增长通常为 2~3 倍，且聚并后的大颗粒主要分布在料锥中部和外部；而导致该现象出现的原因是较高的湍流强度和颗粒分布密度、以及天然气燃烧的位置使该位置处颗粒升温熔融、并发生碰撞和聚并。另外，提高分散风与工艺风动量比能使物料颗粒在反应塔内的分布更加均匀，更有利于冰铜的氧化反应。相较于调整工艺风参数，改变分散风能更有效地提高颗粒的空间分布范围。

关键词：工业试验；颗粒演化；质量分布；粒径分布；动量比；闪速吹炼炉

(Edited by Wei-ping CHEN)